**ORIGINAL PAPER**

# Melt inclusions in zircon: a window to understanding the structure and evolution of the magmatic system beneath the Laguna del Maule volcanic field

Kei Shimizu[1,2] · Tyler B. Blum[1] · Chloe E. Bonamici[1] · John H. Fournelle[1] · Christine E. Jilly-Rehak[3] · Noriko T. Kita[1] · Kouki Kitajima[1] · Jacob D. Klug[1] · Will O. Nachlas[1] · Brad S. Singer[1] · Michael J. Spicuzza[1] · Alexander V. Sobolev[4] · Bryan A. Wathen[1] · John W. Valley[1]

## Abstract

Explosive silicic eruptions pose a significant threat to society, yet the development and destabilization of the underlying silicic magmatic systems are still controversial. Zircons provide simultaneous information on the trace element composition and age of silicic magmatic systems, while melt inclusions in quartz and plagioclase yield important constraints on their volatile content as well as magma storage depth. Melt inclusions in zircons (MIZs) combine these data from a single mineral grain, recording the age, storage depth, temperature, and composition of magmas, and thus provide unique constraints on the structure and evolution of silicic magmatic systems. We studied MIZs from the Laguna del Maule (LdM) volcanic field in the southern Andes that is among the most active Pleistocene-Holocene rhyolitic volcanic centers worldwide and a potentially hazardous system displaying inflation rates in excess of 25 cm/yr. The host zircon ages suggest that the LdM MIZ record extends to ~ 30 kyr before eruption, in contrast to the melt inclusions in LdM plagioclase and quartz crystals that formed only decades to centuries before eruption. The major element compositions of MIZs are minimally affected by post-entrapment crystallization, and agree well with the LdM rhyolitic whole rock data. The MIZs record long-term differences in zircon-saturated melt composition between two eruptive units (rdm: Rhyolite of the Laguna del Maule vs. rle: Rhyolite of Los Espejos). The more evolved major element composition of rle MIZs than rdm MIZs, suggests a long-term deeper connection of the rdm crystal mush to a more primitive magma body than that of the rle. The evidence of slow H diffusion observed in MIZs suggest that their $H_2O$ contents are not significantly affected by diffusion of H through the host zircon. The magma storage pressures of 1.1 to 2.8 kbars recorded by the $H_2O$ contents of rdm and rle MIZs are consistent with the optimal emplacement window ($2.0 \pm 0.5$ kbar) of silicic magma reservoir growth, storage, and eruptibility based on thermomechanical modeling (Huber et al. 2019).

**Keywords** Zircon · Melt inclusions · Rhyolite · Laguna del Maule · Andes

## Introduction

Silicic magmatic systems can generate explosive eruptions of moderate to large sizes ($< 1$ to $> 10^3$ km$^3$), posing significant risks to local communities and potentially causing substantial disruptions to global climate patterns that can adversely affect human societies and natural ecosystems. Shallow silicic magmas are thought to reside in the crust in the form of a crystal mush comprising less than 50% of melt, making it too viscous to erupt in bulk (Hildreth 2004). The process by which magma reservoirs develop and expand to significant sizes in the shallow crust over thousands of years, as well as the factors that cause destabilization, unrest, and

eruption, is a topic of debate (Mahood 1990; Bachmann and Bergantz 2004; Bindeman and Simakin 2014; Wolff et al. 2015). The emerging model of trans-crustal magmatic systems suggests that sub-volcanic magma storage and differentiation occurs within multiple mushy magma reservoirs distributed vertically throughout the crust (Cashman et al. 2017).

Zircons have the unique ability to provide simultaneous information on the trace element composition and age within a single crystal domain by in situ microanalytical techniques (e.g., Claiborne et al. 2010; Reid et al. 2011). The examination of zircon ages and compositions in silicic systems has revealed a variety of processes, such as long-term magma accumulation ($10^3$–$10^4$ years), the merging of magmas with differing compositions, and the remobilization of near-solidus silicic magma (e.g., Bindeman et al. 2008; Wilson and Charlier 2009; Charlier and Wilson 2010; Barker et al. 2014; Chamberlain et al. 2014; Wotzlaw et al. 2015; Reid and Vazquez 2017). Zircons have also provided constraints on the duration of mobile and eruptible magma storage prior to eruption, although conflicting observations have been made based on trace element diffusion profiles in zircon that suggest eruptible magmas are a transient feature in a predominantly cool, crystalline, and largely subsolidus crystal mush (Cooper and Kent 2014; Rubin et al. 2017; Szymanowski et al. 2017), while Ti-in-zircon temperatures suggest storage of eruptible magma for a $10^3$–$10^4$ year time scale (Barboni et al. 2016).

Eruptible rhyolite can be extracted via gravitational compaction and hindered settling (Bachmann and Bergantz 2004), while injections of hotter primitive magma catalyze this process by thermally rejuvenating the crystal-rich magma or remelting the silicic crust and cumulate (Mahood 1990; Bachmann and Bergantz 2004; Bindeman and Simakin 2014; Wolff et al. 2015). Volatiles such as $CO_2$ and $H_2O$ play an important role, as they can transfer heat from a degassing primitive magma to the overlying crystal mush (e.g., Bachmann and Bergantz 2006), promote melt migration through a crystal mush (e.g., Huber and Parmigiani 2018), cause second boiling, inflation of magma reservoir, and explosive behavior (Blundy and Cashman 2008). Melt inclusions in minerals such as quartz and plagioclase provide important constraints on the volatile content of the primitive and more evolved magma, as well as their storage depth (Wallace et al. 1999; Blundy and Cashman 2005; Wallace 2005).

We present major element and $H_2O$ contents of melt inclusions in zircon (MIZs) and the trace element composition and $^{230}Th$-$^{238}U$ ages of the host zircons erupted in the rhyolitic LdM volcanic field. Values of $\delta^{18}O$ are also reported for MIZs and host zircons. LdM volcanic field is among the most active Pleistocene-Holocene rhyolitic volcanic centers worldwide and a potentially hazardous

system showing inflation rates > 25 cm/yr (Singer et al. 2014a). MIZs can record volatile saturation pressure ($H_2O$-$CO_2$ in MIZ), temperature (Ti-in-zircon thermometer), composition (MIZ major and trace element), and time ($^{230}Th$-$^{238}U$ ages) that provide a unique set of constraints on the understanding of the structure and evolution of silicic magmatic systems (e.g., Thomas et al. 2003). Using our data, we distinguish and evaluate the effect of post-entrapment modification versus primary magmatic processes on the MIZ composition through crystallization and diffusive exchange. We then use our data to examine the structure and storage conditions of magma reservoirs at LdM through time.

## Geological setting

The Laguna del Maule volcanic field is located in the Southern Volcanic Zone (SVZ) of central Chile, 30 km behind the active volcanic front (Fig. 1). The volcanism at LdM has been dominantly silicic and concentrated within the central lake basin since the most recent glacial retreat, which is estimated to have occurred locally at c. 23 to 19 ka based on $^{40}Ar/^{39}Ar$ dates of unglaciated lava flows (Singer et al. 2000; Andersen et al. 2017). Both effusive and explosive eruptions at LdM yielded rhyolites that contain less than 10 vol.% phenocrysts of plagioclase, biotite, and magnetite $\pm$ quartz $\pm$ amphibole $\pm$ zircon. The 20 km³ plinian Rhyolite of Laguna del Maule (rdm), thought to have erupted from a vent beneath the modern lake (Fierstein 2018), is the earliest known post-glacial rhyolite. The subsequent rhyolite eruptions, each less than 3 km³ in volume, occurred most frequently during an early post-glacial (EPG) period from 22.5 to 19 ka, and during the middle to late Holocene. Rhyodacite and andesite eruptions also occurred throughout post-glacial times, but comprise a smaller cumulative volume than the rhyolites and were concentrated in the western LdM basin, away from the locus of rhyolite volcanism. Based on these observed spatial relations, Hildreth et al. (2010) proposed that a massive silicic magma reservoir is present below LdM, obstructing the rise of mafic magma.

This hypothesis is increasingly supported by geological, geochronological, and geophysical studies, which suggest that the shallow magma system is still active at present with ongoing average inflation of ~20 cm/year since 2007 (up to 29 cm/year) (Feigl et al. 2014; Le Mevel et al. 2015, 2016; Andersen et al. 2017, 2018; Miller et al. 2017; Cordell et al. 2018; Fierstein 2018; Singer et al. 2018; Wespestad et al. 2019; Le Mével et al. 2021). Both surface- and teleseismic-tomography have shown the presence of a crystal-rich reservoir with 450 to 500 km³ of partial melt at a depth of 2–12 km beneath the northwest portion of the lake at LdM (Wespestad et al. 2019; Bai et al. 2020). Magnetotelluric observation suggests the presence of a deeper partially
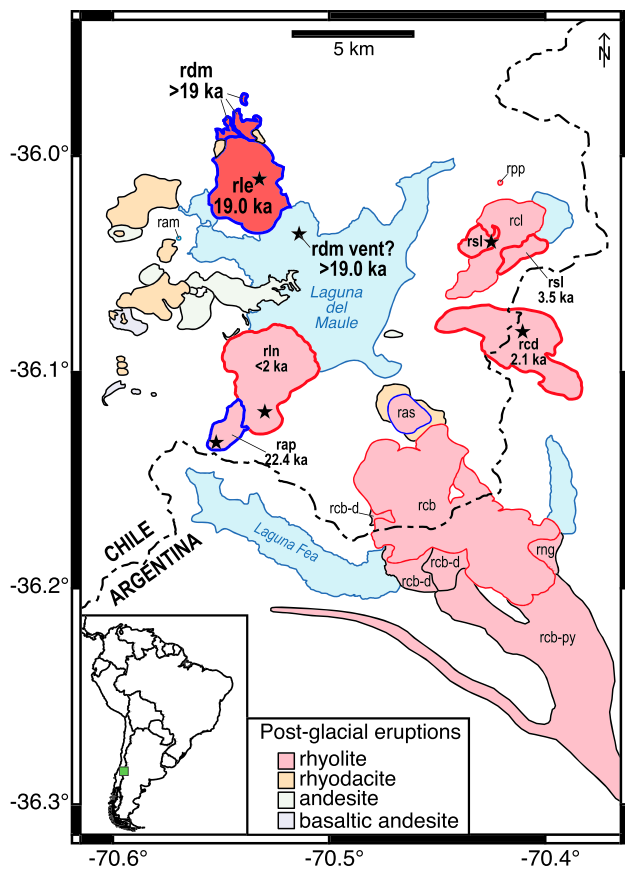
**Fig. 1** Simplified map of the Laguna del Maule lake basin and the distribution of post-glacial eruptive units and vents (black stars). Lava flows and pyroclastic flows/falls that erupted in the early post-glacial period (22.5–19 ka) are outlined in blue, while those that erupted in the Holocene (8.0–1.8 ka) are outlined in red. Those that erupted in the interim are outlined in black. Eruptive units for which MIZ data were obtained (rdm and rle units in the northwest) are highlighted with darker red fill. Map is modified from Hildreth et al. (2010) and Andersen et al. (2019). The green square in the inset shows the location of Laguna del Maule in the southern Andes

molten reservoir that extends beyond 15 km depth (Cordell et al. 2018, 2019).

Plagioclase trace element compositions as well as plagioclase and quartz melt inclusions have provided constraints on magma extraction processes and magma storage conditions that have not been available from whole rock data (Andersen et al. 2018; Klug et al. 2020). Trace element diffusion modeling of LdM plagioclase suggests a short time scale (decades to centuries) between extraction of crystal-poor rhyolite from crystal mush and its eruption (Andersen et al. 2018). Melt inclusions in plagioclase and quartz revealed shallowing magma storage depth with increasing degree of melt differentiation, with the latter being more evolved and recording lower $H_2O$ contents/shallower storage depth (Klug et al. 2020). Based on these observations, Klug et al. (2020) argued that crystal-poor

rhyolite went through decompression-driven fractional crystallization as it ascended from ~ 14 km to ~ 4 km shortly before eruption.

Zircon petrochronology records up to 160 kyr of rhyolitic magma production in the crystal mush reservoir of the LdM (Andersen et al. 2019). The significant age difference between plagioclase and quartz (decades to centuries) compared to zircon has been attributed to extraction of rhyolite from a crystal mush entraining smaller zircons preferentially over larger crystals of major phases (Claiborne et al. 2010; Stelten and Cooper 2012; Andersen et al. 2019). Based on the Ti-in-zircon thermometry as well as modeling of zircon crystallization rates, contemporaneous existence of hot zones and regions of cold storage within the mush reservoir has been hypothesized (Andersen et al. 2019).

## Samples and Methods

### Samples

The sample that is the main focus of this study is from the 20 $km^3$ plinian rdm unit (22.5 to 19 ka) that comprises ash and pumice lapilli (up to 4 cm in diameter) from quickly cooled tephra within well-defined stratigraphic sections (Klug et al. 2020). We report data from an additional sample of the Los Espejos rhyolite (rle) unit, which erupted at $19.0 \pm 0.4$ ka subsequent to rdm (Andersen et al. 2017).

### Mount preparation

A ~ 2 kg pumice sample of the rdm unit was crushed and sieved into $\geq 250$ μm and $< 250$ μm size fractions. Approximately 1000 zircon grains were separated from the $< 250$ μm fraction using conventional techniques including Wilfley-type shaking table, Frantz isodynamic magnetic separator, and heavy liquid separation. The zircon grains were then handpicked, cast in epoxy grain mounts, and polished. At least two grains each of UWZ-1 zircon (Valley et al. 2024) and UWQ-1 quartz (Kelly et al. 2007) standards were also cast in the same mount. The relief between the grains and adjacent epoxy was minimized to $< 1$ μm and grains were placed in the central 8 mm radius region of the mount to ensure good spot-to-spot reproducibility (Kita et al. 2009; Peres et al. 2013). In addition to the epoxy mount, we also studied a mount with LdM zircons that was prepared and analyzed by Andersen et al. (2019) who pressed the zircon grains into soft indium and analyzed euhedral crystal faces for trace elements and $^{230}Th$-$^{238}U$ isotope ratios. The indium mount was then polished to expose the crystal interiors which were also analyzed for trace elements and $^{230}Th$-$^{238}U$ isotope ratios by Andersen et al. (2019). The MIZs exposed

in these zircons were studied here, which are all from the rle unit.

## Imaging of zircons/MIZs

Zircons were imaged by reflected light, backscattered electrons (BSE), and cathodoluminescence (CL) using a Hitachi S-3400N Scanning Electron Microscope (SEM) and Gatan Chroma CL system at the University of Wisconsin–Madison. For both the epoxy and indium mounts, we focused only on zircons that have MIZs. The crystal sizes range from 57 to 174 µm on the long axis and 26 to 88 µm on the short axis with aspect ratios of 1 to 3.3 (Figs. 2 and S1). Zircon morphologies range from anhedral to euhedral and prismatic and all the crystals are clear and colorless. In CL, the zircons are characterized by sector and oscillatory zoning. Around some melt/mineral inclusions, the host zircon is characterized by undulating CL pattern and/or bright CL (Fig. S1).

All zircon grains were imaged by BSE to look for MIZs exposed at the grain surface. A potential issue to this approach is that some of the 3D context of the MIZ and host zircon is lost from the polishing process of exposing the MIZ. This limits certain characterization of the MIZs such as their volume and dimensions, their spatial distribution within the host zircon, as well as the potential presence of vapor bubbles and crystals (e.g., Sobolev and Kostyuk 1975; Roedder 1984; Bodnar and Student 2006; Rose-Koga et al. 2021) in the MIZs that may have been polished away. Despite the loss of certain 3D context, it is highly unlikely that the MIZs were embayment/melt channel that were in contact with the surrounding melt based on the clearly distinct $H_2O$ content and major element composition of the MIZs compared to those of the surrounding melt (i.e., matrix glass) (Sects. "Major Elements" and "$H_2O$ Contents") indicating lack of communication between the MIZs and the surrounding melt.

Qualitative analyses of major elements of MIZs were done by an Oxford AZtecOne energy-dispersive X-ray spectroscopy (EDS) system with acceleration voltage and beam current of 15 kV and 1 nA, respectively. We carefully selected MIZs that are glassy and homogeneous. We also avoided MIZs that are visibly intersected by cracks in the host zircon. The nineteen MIZs identified in 17 rdm zircon grains range from 8 to 25 µm on the long axis and 5 to 14 µm on the short axis with aspect ratios of 1.1 to 5.3 (Figs. 2 and S1). Six MIZs found in the rle zircons range from 5 to 43 µm on the long axis and 3 to 5 µm on the short axis with aspect ratios of 1.1 to 8.7 (Figs. 2 and S1). On the exposed surface, all 25 MIZs are glassy and 20 are completely homogeneous while 5 of them are mostly homogeneous except small microcrystals of titanomagnetite and pyroxene (not shown). Nineteen of the MIZs are circular to oval in shape, while

six are elongated to irregularly shaped. Four out of 17 rdm zircon grains have matrix glass adhered onto them.

## EPMA of MIZs

Chemical composition of the MIZs was measured with a CAMECA SXFive Field Emission Electron Probe Microanalyzer (FE-EPMA) at the Department of Geoscience at the University of Wisconsin–Madison. The sample mounts were coated with a 20 nm carbon layer after being cleaned with distilled water and ethanol. Analyses were conducted with an accelerating voltage of 15 kV, a beam current of 1 nA, and a beam diameter of 2 or 3 µm. The low beam current was selected to minimize beam induced element migration during the EPMA measurements. Major elements (Na, Al, Si, Mg, K, Ca) were measured for 200 s and quantified using Mean Atomic Number (MAN) background regression (Donovan et al. 2016). Oxygen and the remaining minor elements (P, Fe, Mn, Ti, Zr) were quantified using off-peak background regression and measured for 60 s on peak and 30 s on each high and low background position. An exponential background regression was used for analysis of O. Time-dependent intensity corrections were applied for Na, K, Si, and O. Analysis of hydrous haplogranite glass (6.6 wt% $H_2O$; Morgan and London 2005) was used to evaluate accuracy of the analytical routine. Many of the zircon MIZs had diameter < 5 µm. This resulted in secondary fluorescence of Zr from the surrounding zircon matrix. Monte-Carlo simulation of electron-specimen interactions using PENEPMA was used to constrain the extent of secondary fluorescence for various inclusion dimensions and beam diameters. Addition of Zr into the analysis routine was used to monitor the effects of secondary fluorescence on individual measurements; any measurements with > 1 wt% $ZrO_2$ were interpreted as affected by secondary fluorescence and discarded from consideration. For MIZ analyses with < 1 wt.% $ZrO_2$, the compositions were corrected to be $ZrO_2$-free, assuming essentially all Zr signal was from host zircon.

## SIMS

### Zircon $\delta^{18}O$; MIZ $\delta^{18}O$ and $H_2O$

Zircon oxygen isotope ratios as well as MIZ oxygen isotope ratios and $H_2O$ contents were measured using the CAMECA IMS-1280 secondary ion mass spectrometer (SIMS) at the WiscSIMS laboratory at the University of Wisconsin–Madison. The zircon epoxy mount was gold-coated after being cleaned with distilled water and ethanol and kept in a vacuum oven at 60ºC for 24 h. Zircon analyses were made following the methods described previously (Kita et al. 2009; Valley and Kita 2009; Wang et al. 2014). A primary $^{133}Cs^+$ ion beam was focused to 10 µm diameter
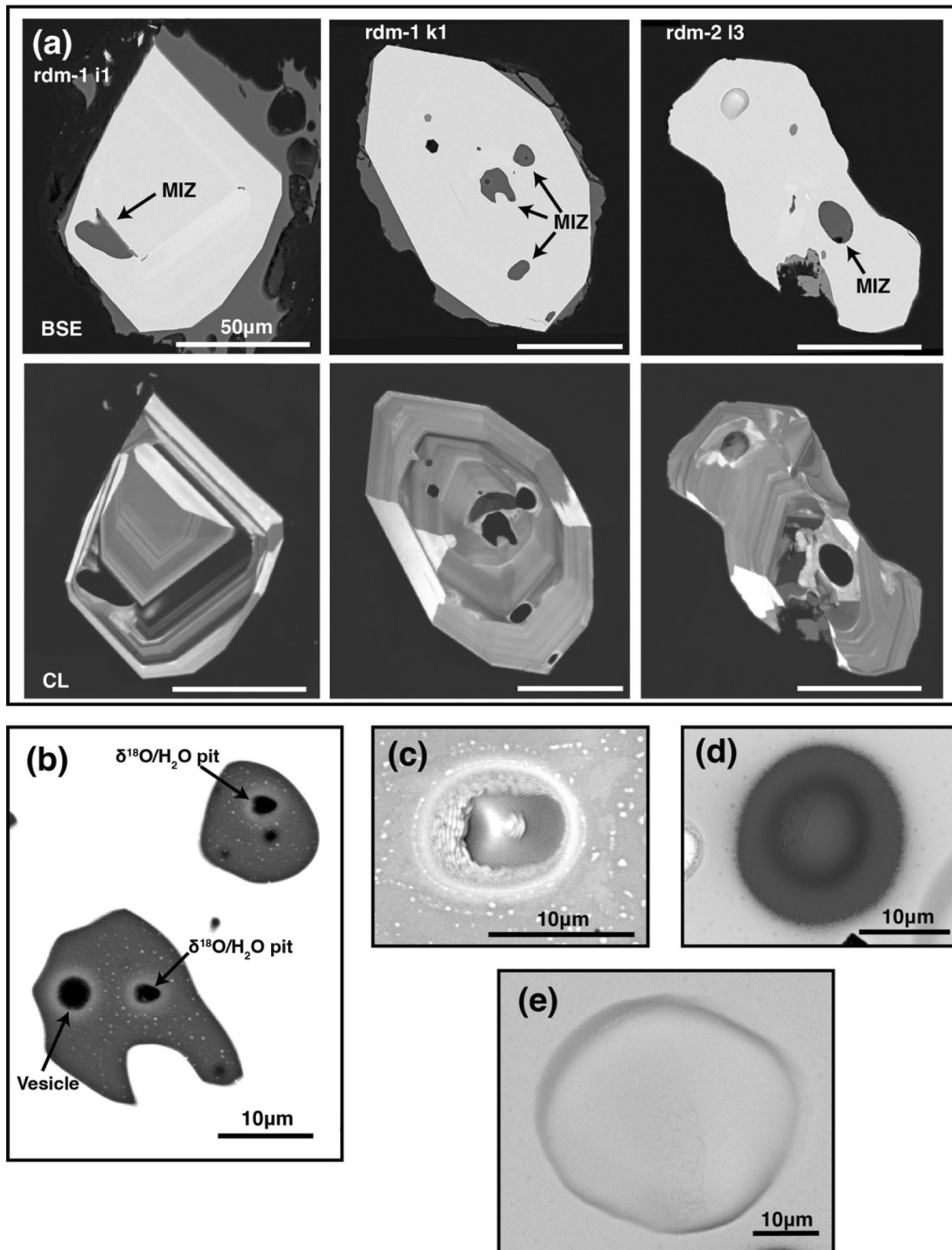
**Fig. 2** **a** BSE and CL images of representative MIZs/host zircons (scale bars = 50 μm). **b** BSE image of SIMS pits and Cs spatter from the analyses of $\delta^{18}O/H_2O$ of the MIZ (~3 μm diam.). **c** and **d** BSE images of SIMS pits from the analyses of $\delta^{18}O$ (~10 μm diam.) and trace element (~13 μm diam.) of the zircons, respectively. **e** BSE image of a SHRIMP pit from the $^{238}U-^{230}Th$ age dating of the zircons (~40 μm diam.)

with an intensity of 1.7 to 1.8 nA, to generate $\sim 3 \times 10^9$ counts per second (cps) of secondary $^{16}O^-$ ions. The multicollection (MC) Faraday cup (FC) detectors were used to simultaneously measure $^{16}O^-$, $^{18}O^-$, and $^{16}O^1H^-$ signals with feedback resistors of $10^{10}$, $10^{11}$, and $10^{11}$ Ω, respectively. Individual zircon analyses lasted approximately 3.5 min including sputtering of the gold coated surface (10 s), automatic centering of the secondary ion beam in the field aperture (60 s), and 40 cycles of 4 s integrations of oxygen ion measurements. Analysis pits were $\sim 2$ μm deep. For the MIZ analysis, the primary $Cs^+$ ion beam was focused to 3 μm diameter with an intensity of 25 pA, to generate $\sim 3.5 \times 10^7$ counts per second (cps) of secondary $^{16}O^-$ ions. Each MIZ analyses lasted approximately 4 min including sputtering of the gold coated surface (30 s), automatic centering of the secondary ion beam in the field aperture (60 s), and 20 cycles of 8 s integrations of oxygen ion measurements. The $^{16}O^-$ and $^{18}O^-$, and $^{16}O^1H^-$ signals were measured simultaneously in two FCs ($^{16}O^-$ and $^{16}O^1H^-$, both with feedback resistors of $10^{11}$ Ω) and one electron-multiplier (EM) for $^{18}O^-$ ($\sim 7 \times 10^4$ cps). Hydride interferences at mass 18 were resolved at mass resolving power (MRP at 10% peak height) of 2,200, and MRP of 5,000 was used for mass 17 to resolve $^{16}O^1H^-$ from $^{17}O^-$. A liquid $N_2$ trap was used to maintain vacuum in the sample chamber $\leq 5 \times 10^{-9}$ mbar to reduce hydrogen background. Four analyses of UWZ-1 zircon standard were made at the beginning of the session and after every 10 unknowns. The bracketing sets of eight analyses of UWZ-1 ($\delta^{18}O = 4.98$ ‰ VSMOW) were used to monitor instrumental bias for zircon standard and the spot-to-spot reproducibility for individual brackets, which ranged between 0.17 and 0.21 ‰ (2SD) for the zircon analyses and 0.51 to 0.75 ‰ (2SD) for the MIZ analyses.

For $H_2O$ contents of MIZs, calibration was made between the measured $^{16}O^1H^-/^{16}O^-$ and $H_2O$ content using rhyolitic glass standards with known $H_2O$ concentrations (Newman et al. 1986; Singer et al. 2014b; Klug et al. 2020). The major element compositions of these rhyolitic glass standards encompass those observed in the MIZ (Fig. S2). For the February 2022 session, we obtained a linear regression line between $^{16}O^1H^-/^{16}O^-$ versus $H_2O$ wt.% (0.33 to 3.51 wt.% $H_2O$ rhyolitic glasses; Newman et al. (1986), Klug et al. (2020)) (Fig. S3a, Table S2). The majority of MIZ $H_2O$ contents obtained during this session were beyond the calibration range (> 3.5 wt.%). A subsequent session in June 2022 was conducted, in which we measured higher $H_2O$ content standards (0 to 6.09 wt.% $H_2O$ rhyolitic glasses; Singer et al. (2014b)). We obtained a polynomial regression line between $^{16}O^1H^-/^{16}O^-$ versus $H_2O$ wt.% (Fig. S3b, Tables S3). The $H_2O$ contents of MIZs that were analyzed during both February 2022 and June 2022 sessions agree to within 10% on average (Fig. S3c). For both sessions, the background levels of $^{16}O^1H^-/^{16}O^-$ were

determined by multiple analyses of the UWZ-1 zircon grains, which were subtracted from the $^{16}O^1H^-/^{16}O^-$ of the melt inclusion analyses before converting them to $H_2O$ wt.%. The background corrections were typically smaller than 10% of measured $^{16}O^1H^-/^{16}O^-$ values. To correct for MIZ $\delta^{18}O$ instrumental mass fractionation, anhydrous glass standards with known $\delta^{18}O$ (Jochum et al. 2006) were analyzed that have a range of $SiO_2$ from 51.4 to 75.6 wt.% (Tables S2 and S3). The $\delta^{18}O$ bias was estimated relative to zircon (bias*) as a function of the $SiO_2$ content of the glass standards. The $\delta^{18}O$ of individual MIZs were corrected for the bias based on the bias estimated from bracketing zircon standard analyses and the relative bias (bias*) of each MIZ that is calculated using the $SiO_2$ content (EPMA data). The effect of $H_2O$ on the MIZ $\delta^{18}O$ instrumental mass fractionation was evaluated using some of the aforementioned hydrous rhyolitic glass standards as well as hydrous basaltic glass standards that had previously been analyzed for $\delta^{18}O$ (Newman et al. 1988; Eiler et al. 2000). This showed that the instrumental biases of the hydrous glasses agree well with those of the anhydrous glasses such that the effect of $H_2O$ on the MIZ $\delta^{18}O$ instrumental mass fractionation is minimal.

### Zircon trace elements

Zircons were analyzed for 26 trace elements (Al, P, Ca, Sc, Ti, Fe, Y, Nb, La, Ce, Pr, Nd, Sm, Eu, Gd, Tb, Dy, Ho, Er, Tm, Yb, Lu, Hf, Ta, Th, U) using the CAMECA IMS-1280 secondary ion mass spectrometer (SIMS) at the WiscSIMS laboratory at the University of Wisconsin–Madison. Analyses used a $^{16}O^-$ primary beam at a current of 5.4 nA and a total impact energy of 23 kV (–13 kV at the ion source and + 10 kV on the sample surface). Analytical pits were $\sim 13$ μm in diameter. The mass spectrometer was operated at a nominal mass resolving power (MRP = M/ΔM) of 14,000, which allows for separation of $^{45}Sc^+$ and $^{93}Nb^+$ from interferences with $^{90}Zr^{++}$ and $^{92}ZrH^+$, respectively (e.g., Grimes et al. 2015; Coble et al. 2018; Blum et al. 2023). No energy offset was applied because most molecular interferences, such as REE oxides on REE, were fully resolved. Each analysis included a 30 s pre-sputter, centering of the secondary beam within the field aperture, and five cycles of counting from low to high mass by magnetic peak-jumping on axial mono-collector (mostly EM except for major element Si and Zr peaks on FC). Normalized count rates (normalizing species $^{28}Si$) are converted to trace element concentrations based on element specific relative sensitivity factors (RSFs). RSFs were determined for the primary reference material, NIST610 (Pearce et al. 1997) with correction factors based on multiple zircon reference materials to account for matrix mismatch between glass and zircon, similar to those in previous studies (Page et al. 2007; Bouvier et al. 2012; Kitajima et al. 2012). Zircon reference

materials analyzed in this study are 91500 (Wiedenbeck et al. 2004; Coble et al. 2018), MAD-559 (Coble et al. 2018), and GZ7 (Nasdala et al. 2018). For elements (Al, Ca, Sc, and Fe) that do not have homogeneous or well characterized published values in the reference material suite, no correction factor is applied (Wiedenbeck et al. 2004; Coble et al. 2018). Additional analytical details will be published elsewhere.

### Zircon $^{230}$Th-$^{238}$U

To prepare the zircon epoxy grain mount for SIMS U-Th analyses, the mount was cleaned with a 10% EDTA (ethylenediaminetetraacetic acid) wash, thoroughly rinsed with DI water, then given a quick ~ 30 s rinse in 1 M HCl to remove surface contamination before being dried at 50 °C in a vacuum oven for 30 min. The sample surface was coated with ~ 10–20 nm of gold for conductivity before being loaded in the instrument sample lock chamber.

Zircon U-Th analyses were conducted on the SHRIMP-RG (reverse geometry) ion microprobe in the co-operated Stanford and U. S. Geological Survey SUMAC facility at Stanford University. Analytical procedure and data reduction follows methods developed by Williams (1997) and Ireland and Williams (2003). An $O_2^-$ primary beam with accelerating voltage of 10 kV was used to sputter secondary ions from the sample surface with a ~ 19 nA primary beam current focused to ~ 42 μm. Prior to analysis, spots were presputtered for 60 s remove gold coating and surface contamination from the analysis area, and the primary and secondary beams were auto-tuned to maximize transmission. Seven masses were measured, including $^{90}Zr_2^{16}O$, $^{238}U^+$, $^{232}Th^{12}C^+$, $^{230}Th^{16}O^+$, background measured 0.050 AMU above the $^{230}Th^{16}O^+$ peak, $^{232}Th^{16}O^+$, and $^{238}U^{16}O^+$. An energy slit set to 1 mm width was employed to reduce interferences. Data were collected over 8 scans per spot, for a total run time of 33 min, collected by magnet peak-jumping on an EPT discrete-dynode electron multiplier. Mass resolution (M/ΔM) was set to ~ 8000 for all masses, sufficient to resolve any interfering molecular species.

Zircon U concentration data were standardized against the well-characterized MAD-559 (3940 ppm U; Coble et al. 2018) and MAD-1 zircon standards (Barth and Wooden 2010) measured from a separate mount that was co-loaded in the analysis chamber. $(^{238}U)/(^{232}Th)$ and $(^{230}Th)/(^{232}Th)$ ratios were calculated using $\lambda_{238} = 1.55125 \times 10^{-7}$ ka$^{-1}$ (Jaffey et al. 1971), $\lambda_{232} = 4.9475 \times 10^{-8}$ ka$^{-1}$ (Steiger and Jäger 1977), $\lambda_{230} = 0.0091705$ ka$^{-1}$ (Cheng et al. 2013). The $(^{238}U)/(^{232}Th)$ was also corrected for instrument mass fractionation using early-erupted Bishop Tuff (767.1 ± 0.9 ka, Crowley et al. 2007), which is relatively high-U (1000–4000 ppm) and old enough that the U-Th is in secular equilibrium. For analyses measured in this session

$(^{230}Th)/(^{238}U) = 0.8461 \pm 0.0069$ (1σ, n = 9, MSWD = 2.2), which is the RSF that was applied to the unknowns. Data was reduced using the Microsoft Excel add-in programs Squid2.51 and Isoplot3.764 of Ken Ludwig (Ludwig 2001; 2003).

## Results

### $^{230}$Th-$^{238}$U ages of the LdM zircons

We determined the $^{230}$Th-$^{238}$U ages of 11 rdm zircons, ranging from 18.7 ka to secular equilibrium (> 350 ka) (Fig. 3). Out of the 11 rdm zircon grains that were dated, four of them (hereafter referred to as younger rdm zircons) have non-secular equilibrium ages that range from 18.7 to 47.0 ka, falling within the $^{230}$Th-$^{238}$U ages (18.1 to 78.8 ka) previously determined for the zircons from the same unit (Andersen et al. 2019). The youngest zircon age is $18.7^{+5.0}_{-4.7}$ (1SD) ka, which agrees well with the eruption age of the rdm unit (19–23 ka based on field relationships). The remaining seven rdm zircon grains are in secular equilibrium indicating unresolvable ages that are > 350 ka (hereafter older rdm zircons). The six rdm zircon grains that could not be dated (hereafter no age (NA) rdm zircons) either due to the size or SHRIMP beam overlapping epoxy are not included in further discussion given the difficulty in putting them in context of other
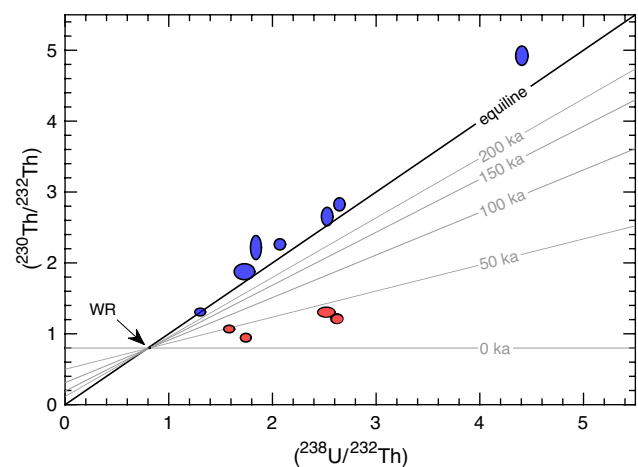


**Fig. 3** $^{238}$U–$^{230}$Th isochron diagram for zircons from the rdm unit of the LdM. Each ellipse represents a SHRIMP-RG analysis of a spot in separate zircon grains. Error ellipses are 1SD. Red ellipses are analyses on the younger rdm zircons (non-secular equilibrium ages), while the blue ellipses are analyses of older rdm zircons (secular equilibrium ages). The small black dot represents the whole rock composition used to calculating the model ages (average of post-glacial rhyolite whole rock data from Andersen et al. (2017)). The heavy black line represents the equiline, while the gray lines represent isochrons of ages from 0 to 200 ka. Some older rdm zircons plot above the equiline, which is likely due to the primary beam overlapping with the epoxy that causes elevated $^{230}$ThO$^+$ background

data without their $^{230}$Th-$^{238}$U ages. For the rle zircons, the previously determined $^{230}$Th-$^{238}$U ages range from 14.9 to 80.8 ka, and those with MIZs found in this study are 19.7 to 48.3 ka (Andersen et al. 2019). No MIZ was found in the rle zircon that is in secular equilibrium.

## Major elements

The major element composition of the younger rdm MIZs are all rhyolitic (75.1 to 76.6 wt.%) and relatively homogeneous (Fig. 4). Their composition agrees well with the tight array defined by the whole rock data of the post-glacial silicic units (Hildreth et al. 2010; Andersen et al. 2017). Their composition is less evolved compared to the rdm whole rock data (Hildreth et al. 2010; Andersen et al. 2017) and the rdm matrix glasses (Contreras et al. 2022) (Fig. S4). The younger rdm MIZs agree well with the most evolved side of the compositional range defined by the rdm plagioclase melt inclusions, which show significant range in $SiO_2$ (71 to 76 wt.%) (Fig. S4). However, the younger rdm MIZs are less evolved compared to the rdm quartz melt inclusions (Klug et al. 2020) (Fig. S4).

In contrast to the younger rdm MIZs, the major element composition of older rdm MIZs are rhyodacitic to rhyolitic, significantly more heterogeneous, and for the most part do not agree well with those of the rdm whole rock/melt inclusions nor with those of the post-glacial silicic units (Andersen et al. 2017) (Fig. 4). The post-glacial whole

rock data form a tight array of chemical data, while the whole rock composition of older units (> 25 ka) is more scattered (Fig. S5). Some of the older rdm MIZs agree with the composition of these older units (Hildreth et al. 2010). However, many of the older rdm MIZs are anomalous (e.g., those with high $K_2O$ of > 6 wt.%) even compared to the whole rock composition of the older eruption units. While there may be a tendency for CL pattern of zircons surrounding older rdm MIZs to have more complex patterns (Fig. S1), clear correlation between MIZ composition and surrounding zircon CL pattern were not observed.

Similar to the younger rdm MIZs, the major element composition of the rle MIZs agree well with the trend defined by the whole rock data of the post-glacial silicic units (Andersen et al. 2017) (Fig. 4). The three less evolved rle MIZs are compositionally similar to the rle whole rock data (Hildreth et al. 2010; Andersen et al. 2017) and rle matrix glasses (Contreras et al. 2022), while the other 3 rle MIZs are more evolved ($SiO_2$ = 77 to 78 wt.%) (Figs. 4 and S6). The more evolved rle MIZs are compositionally similar to the rle plagioclase melt inclusions, most of which are similarly evolved ($SiO_2$ = 76 to 78 wt.% for 11 out of 12 plagioclase melt inclusions) (Klug et al. 2020) (Fig. S6).

## H$_2$O contents

The $H_2O$ contents of the younger rdm MIZs span 4.1 to 5.7 wt.%, and they agree well with those of the rdm plagioclase
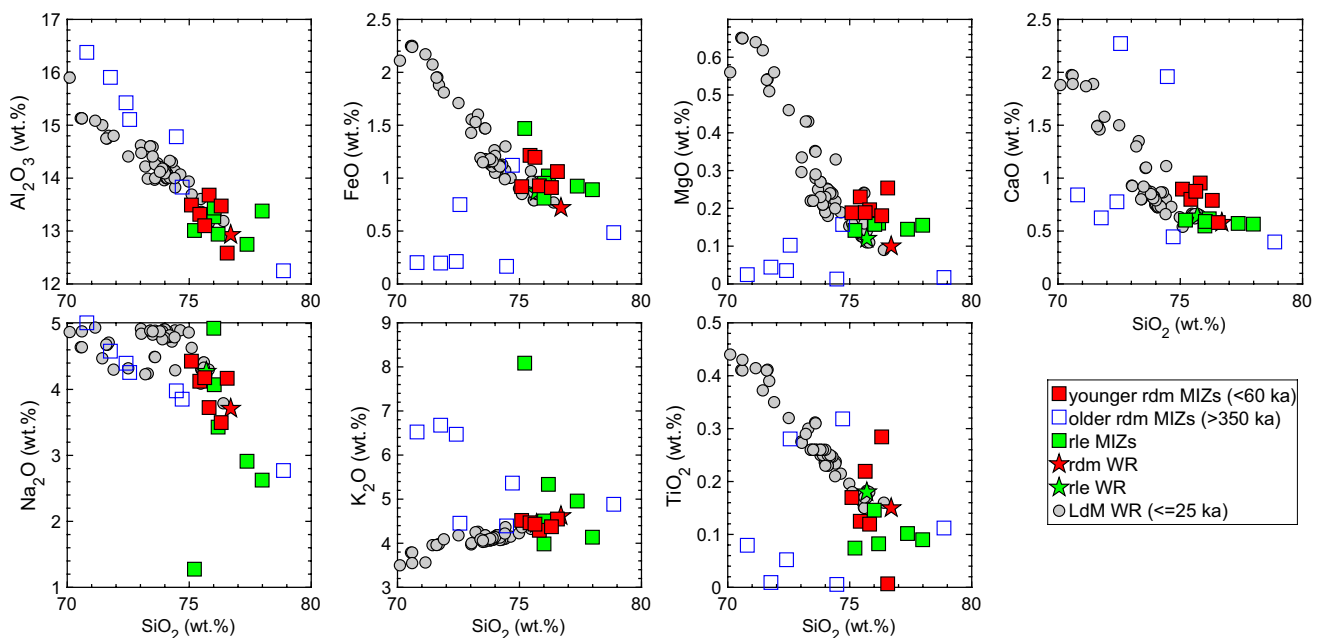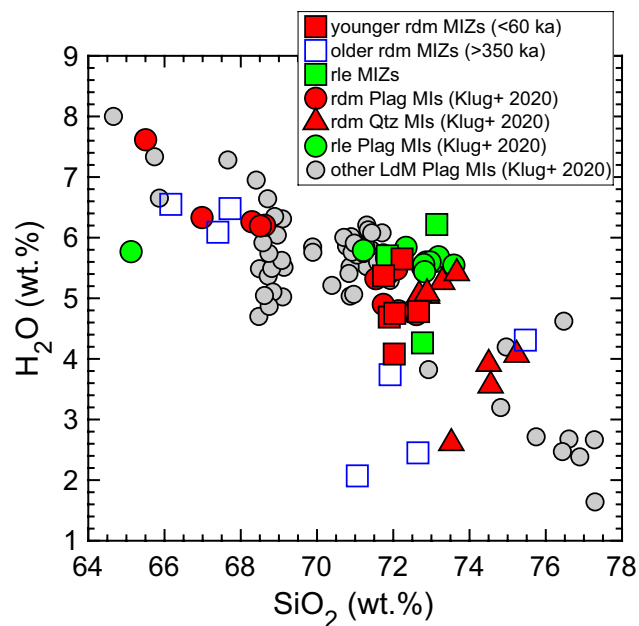


**Fig. 4** Harker diagrams showing the major element composition of the rdm and rle MIZs and correlated whole rock compositions. Whole rock data of younger units (<=25 ka) are from Andersen et al. (2017), Hildreth et al. (2010), and Contreras et al. (2022). MIZ com-positions are normalized to 100% on anhydrous basis to allow direct comparison with the whole rock data. The matrix glass, and melt inclusions in plagioclase and quartz, and the whole rock composition of older units (> 25 ka) are not shown for clarity

melt inclusions (Klug et al. 2020) (Fig. 5). In contrast, the $H_2O$ contents of older rdm MIZs are significantly scattered (2.1 to 6.6 wt.%) compared to the range observed in the rdm plagioclase melt inclusions, reaching similarly low $H_2O$ contents as some quartz melt inclusions (Klug et al. 2020) (Fig. 5). A measurement of the matrix glass adhered onto
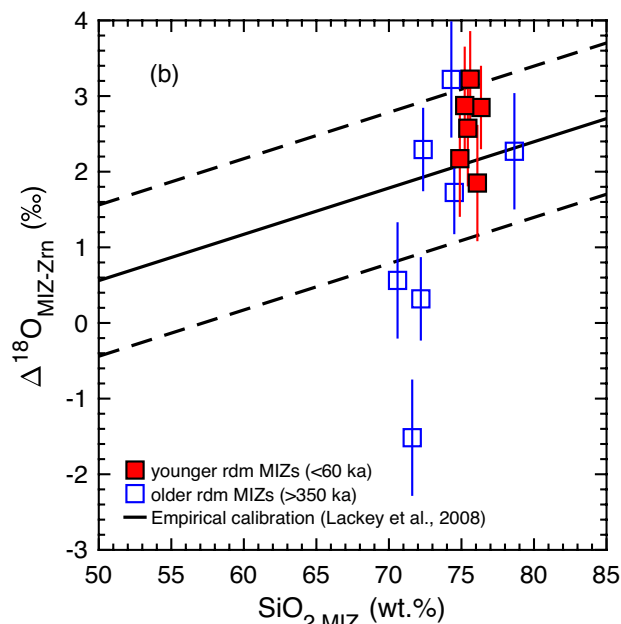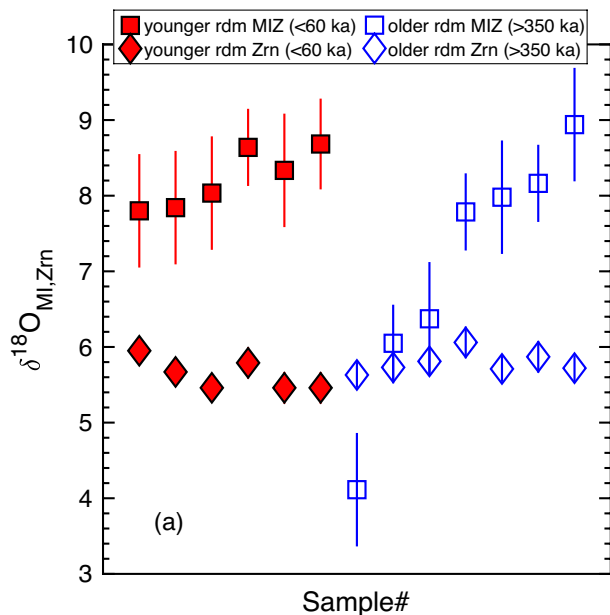
an undated rdm zircon (zircon f4) yielded a distinctly lower $H_2O$ content of 0.05 wt.% in comparison to MIZs. The $H_2O$ contents of the rle MIZs (4.3 to 6.2 wt.%) are comparable to the younger rdm MIZs, although extending to slightly higher $H_2O$ contents. These $H_2O$ contents are comparable with those in the rle plagioclase melt inclusions (5.4 to 5.8 wt.%) (Klug et al. 2020).

## Oxygen isotope ratios

Oxygen isotope ratios of the rdm zircons are homogeneous regardless of age (i.e., younger or older rdm) ($\delta^{18}O = 5.76 \pm 0.32$ ‰, 2SD) (Fig. 6a). The $\delta^{18}O$ values of younger rdm MIZs are also homogeneous ($\delta^{18}O = 8.22 \pm 0.80$ ‰, 2SD), while that of older rdm MIZs is highly variable ($\delta^{18}O = 4.1$ to $8.9$ ‰) (Fig. 6a). The oxygen isotopic fractionation between the glass in younger rdm MIZ and host-zircon is relatively constant ($\Delta^{18}O_{MIZ-Zrn} = 2.59 \pm 1.01$ ‰, 2SD) (Fig. 6b), and within uncertainty with the equilibrium zircon-melt oxygen isotopic fractionation factor (Lackey et al. 2008). The equilibrium fractionation between zircon and melt is nearly constant at magmatic temperatures (Lackey et al. 2008; Grimes et al. 2011; Bucholz et al. 2017). In contrast, oxygen isotopic fractionation between the older rdm MIZ and host-zircon is highly variable ($\Delta^{18}O_{MIZ-Zrn} = -1.52$ to $3.22$ ‰) (Fig. 6b), and some do not preserve equilibrated values from magmatic conditions. The oxygen isotopic composition of the



**Fig. 5** $H_2O$ and $SiO_2$ contents of the rdm and rle MIZs along with plagioclase and quartz melt inclusions (Klug et al. 2020)



**Fig. 6** **a** $\delta^{18}O$ of the MIZ (squares) and zircon host (diamonds). **b** $\Delta^{18}O_{MIZ-Zrn}$ vs. $SiO_2$ content of the MIZ. In (**b**), the dashed line shows the predicted melt-zircon equilibrium isotopic fractionation (Valley et al. 2005; Lackey et al. 2008)

rle MIZs/zircons were not determined, due to the lack of suitable oxygen isotope standard grain in the indium mount.

## Ti-in-zircon thermometry

Ti-in-zircon temperatures were calculated using the calibration of Ferry and Watson (2007), which requires the $TiO_2$ activity ($a_{TiO2}$), $SiO_2$ activity ($a_{SiO2}$) and pressure. Following the previous study on LdM zircons of Andersen et al. (2019), we first used the $a_{TiO2}$ of 0.72 obtained based on magnetite-ilmenite equilibrium (Ghiorso and Evans 2008) and an $a_{SiO2}$ of 1 based on the presence of quartz in the LdM rhyolites (Andersen et al. 2017). The effect of pressure was not taken into account, but such effect is relatively small (~50°C/10 kbar). Ti-in-zircon temperatures calculated based on these $a_{TiO2}$ and $a_{SiO2}$ values along with the measured Ti content in zircons span 708 to 839°C (younger rdm = 708 to 792°C, older rdm = 722 to 839°C, rle = 724 to 796°C). These are comparable to the Ti-in-zircon temperatures previously determined for LdM zircons (Andersen et al. 2019) as well as the temperature range of LdM rhyolites estimated based on the Fe-Ti oxide thermometer (Andersen et al. 2017).

## Zircon trace elements

The trace element composition (e.g., U, Hf, Ti, REE contents) of the younger rdm zircons agree well with those that

were previously observed for rdm zircons (Andersen et al. 2019) (Fig. 7). While it is somewhat unexpected given the anomalous major element composition of older rdm MIZs (Fig. 4), the trace element composition of older rdm zircons compares well with other rdm zircons (Fig. 7a). The Ti content of younger rdm zircons range from 5 to 12 ppm, and correlates negatively with their Hf content that ranges from 8,500–10,700 ppm (Fig. S7). The U content of the younger rdm zircons range from 353 to 1,688 ppm, which tends to correlate with the bright and dark CL regions, respectively. The trace element composition of the rle zircons with MIZs ($U_{Zrn}$ = 266–557 ppm, $Ti_{Zrn}$ = 6–12 ppm, $Hf_{Zrn}$ = 8,100–10,700 ppm) are representative of those of the larger rle zircon data set, except for the most U-rich and -depleted zircons (Andersen et al. 2019). The melt in equilibrium with the zircons calculated using the zircon-melt REE partition coefficients (Sano et al. 2002) are consistent with the whole rock data for the LdM post-glacial units (Andersen et al. 2017) (Fig. S8).

## Discussion

### Post-entrapment modification of MIZs

Subsequent to entrapment in the host crystal, melt inclusions can be modified by processes such as devitrification,
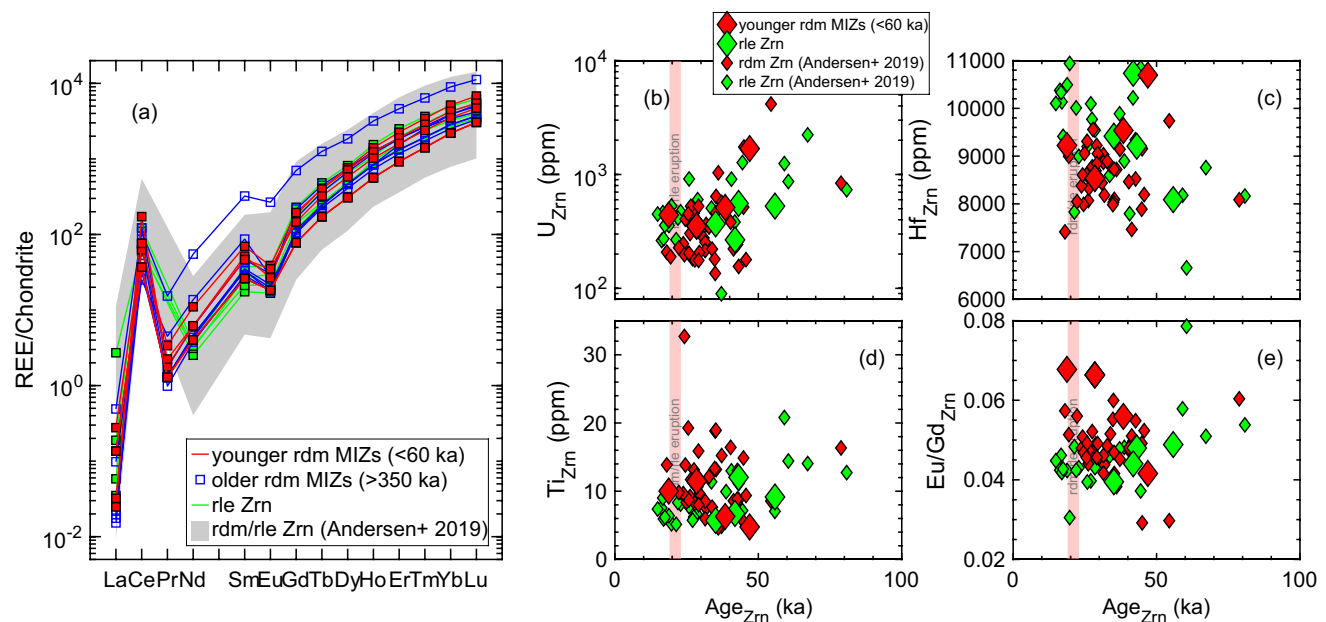


**Fig. 7** **a** Chondrite normalized REE pattern and **b** U, **c** Hf, **d** Ti, and **e** Eu/Gd vs. $^{238}U–^{230}Th$ ages of the rdm and rle zircons. In (**a**) the gray field shows the rdm and rle zircon REE data from Andersen et al. (2019). In (**b**, **c**, **d**, and **e**), older rdm zircons are not shown given their secular equilibrium ages. The large symbols are from this study, while the small symbols are rdm and rle zircon trace element data from Andersen et al. (2019). The vertical light-red bar shows the eruption age of rdm and rle units (Andersen et al. 2017). Chondrite REE values are from McDonough and Sun (1995)

crystallization of new zircon, cracking of host zircon and diffusive exchange with the surrounding melt (e.g., Danyushevsky et al. 2002). However, multiple lines of evidence suggest that post-emplacement processes have had minimal effects on many of the MIZs from rdm and rle units, and that many of the MIZs retain major element, oxygen isotopic composition, and water contents of the entrapped magmas. Post-entrapment crystallization (PEC) (e.g., Kress and Ghiorso 2004) of zircon during cooling is minimal for MIZs given the small concentration of Zr in the melt. For example, LdM whole rocks have a maximum Zr content of 265 ppm (Hildreth et al. 2010), which limits the maximum amount of PEC of zircon to < 0.05 wt.% in a MIZ, assuming Zr content of 500,000 ppm in zircon and that all Zr in the melt is converted to zircon. The effect of PEC of other minerals on the composition of the MIZs in this study is difficult to constrain as we did not conduct heating experiments. However, the younger rdm as well as the rle MIZs in this study have minimal to no textural evidence by SEM of PEC phases given their homogeneous nature (Figs. 2 and S1). Further, the agreement between the major element composition of younger rdm and rle MIZs ($^{230}$Th-$^{238}$U age of host zircon < 60 ka) to those of whole rock data of the post-glacial silicic units (Andersen et al. 2017), as well as those of plagioclase and quartz melt inclusions from the same unit (Klug et al. 2020), suggests that PEC did not have a substantial effect on the younger rdm and rle MIZ compositions (Fig. 4). In contrast, the major element composition of most older rdm MIZs ($^{230}$Th-$^{238}$U age of host zircon in secular equilibrium) significantly deviate from those of whole rock, and plagioclase and quartz melt inclusions, which could be due to the effect of PEC. Nevertheless, the most notable difference in major element composition between younger rdm and older rdm MIZs would require a substantial amount of PEC (e.g., $K_2O$ of 4.4 wt.% in younger rdm MIZ vs. 6.5 wt.% in some older rdm MIZs require ~ 33 wt.% crystallization of quartz) if the original melts were of the same composition. The lack of substantial PEC minerals in SEM images of the older rdm MIZs does not support such large amount of PEC (Figs. 2 and S1). Together with the old age (> 350 ka) of the older rdm MIZs, a more likely explanation is that they formed from a parental melt that formed under magmatic conditions unrelated to those that produced the younger rdm and rle MIZs and other LdM units.

Melt inclusions can record the pre-eruptive volatile contents of magmas. However, after entrapment, volatiles can sometimes diffuse into or out of melt inclusions through the host mineral (e.g., Qin et al. 1992). There are so far no experimental measurements of H diffusion coefficient in zircon under conditions relevant to the LdM zircons (e.g., $f$O$_2$ conditions). In the LdM MIZs, we observe a negative correlation between the degree of differentiation ($SiO_2$) and $H_2O$ contents of MIZs (Fig. 5) that is consistent with those observed in plagioclase and quartz melt inclusions. This negative correlation has been interpreted to suggest decompression-driven fractional crystallization and $H_2O$ degassing as the rdm magma ascended from deeper to shallower portion of the LdM reservoir (Klug et al. 2020). The preservation of such negative correlation in the rdm MIZs strongly suggests the retention of MIZ $H_2O$ contents since the time of entrapment, as diffusive exchange would decouple $H_2O$ from $SiO_2$ in the MIZs. Some older rdm MIZs (> 350 ka) are characterized by low $H_2O$ contents for a given $SiO_2$ (Fig. 5), and may indicate instances of $H_2O$ leakage from these MIZs. With these exceptions aside, we infer that the negative correlation between $SiO_2$ and $H_2O$ contents to indicate that the MIZs in this study were not significantly impacted from diffusive equilibration of H through the host zircon since the time of entrapment.

## Identification of xenocrystic rdm zircons/MIZs (older rdm)

The older rdm zircons that are in secular equilibrium (> 350 ka) host MIZs that are anomalous in composition (Fig. 4). Their compositions do not agree with those of the rdm unit nor other whole rock data of the post-glacial silicic units and older units (Hildreth et al. 2010; Andersen et al. 2017). The older rdm MIZs are generally low in FeO and MgO and also show significantly more variable CaO, $TiO_2$, as well as $H_2O$ contents for a given $SiO_2$ content compared to the younger rdm and rle MIZs and LdM whole rock data (Figs. 4 and 5). Three older rdm MIZs have significantly higher $K_2O$ content than younger rdm and rle MIZs as well as LdM whole rock (Fig. 4). These high $K_2O$ older rdm MIZs have anomalously low $\delta^{18}$O values that are not in isotopic equilibrium with the host zircon (Fig. 6b). While the distinct major element composition could in part be due to post-entrapment crystallization of certain phases, high $K_2O$ contents and anomalously low $\delta^{18}$O observed in some MIZs are difficult to explain by such process. Taken together with their secular equilibrium ages (> 350 ka), we hypothesize that older rdm zircons/MIZs are xenocrystic in origin and that the MIZs record older exotic melt compositions that formed under magmatic conditions unrelated to those that produced the rdm and rle eruptions. The highly variable $H_2O$ content of older rdm MIZs also supports this hypothesis. Our observation shows the importance of age dating the host zircon in order to avoid xenocrystic zircons that may host MIZs with chemical composition that is irrelevant to the magmatic system of interest. In terms of the origin of the older rdm zircons, they may have originated from deeper granites that are represented by crustal xenoliths found in the pyroclastic flow facies of the rdm unit. These are exceptionally large (up to ~ 1 m) crustal debris with

heterogeneous lithologies that could be Pliocene-Miocene plutonic rocks that housed the magmatic precursor to the more recent LdM system, analogous to those observed in the Risco Bayo-Huemul plutonic complex 20 km west of the LdM system (Schaen et al. 2018, 2021). The other post-glacial units including the rle do not contain such granitoid xenoliths. The rdm unit is exceptional in this regard, which explains the uniquely high abundance of secular equilibrium age zircons in the rdm units compared to other units including the rle unit.
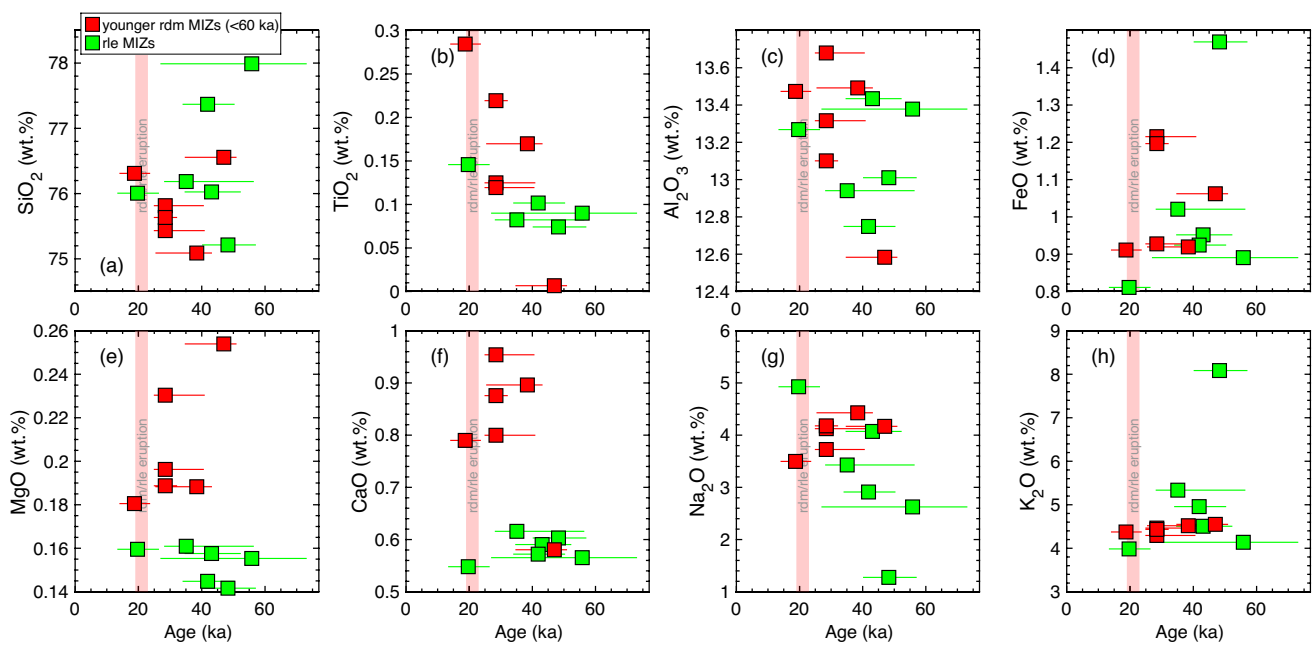
## Major element composition and $H_2O$ contents of the younger rdm and rle MIZs: Implications for the LdM magmatic system

In contrast to the older rdm zircons and MIZs, the geo-chemical data of the younger rdm zircons and MIZs are consistent with their formation from the active magmatic system that underlies the LdM. The $^{230}Th$-$^{238}U$ ages of $18.7^{+5.0}_{-4.7}$ to $47.0^{+4.0}_{-3.9}$ (1SD) ka for the younger rdm zircons agrees with the previously determined $^{230}Th$-$^{238}U$ ages (18.1 to 78.8 ka) of the rdm unit zircons (Andersen et al. 2019). All younger rdm MIZs are in oxygen isotopic equilibrium with their host zircon (Fig. 6b). The major element compo-sitions of younger rdm MIZs are akin to those of the whole rock data for the rdm unit as well as other post-glacial LdM units (Hildreth et al. 2010; Andersen et al. 2017), matrix glasses (Contreras et al. 2022), and plagioclase/quartz melt inclusions (Klug et al. 2020) (Figs. 4 and S4). The $SiO_2$ contents of these younger rdm MIZs are consistent with the predicted $SiO_2$ content ($> 70$ wt.%) above which the LdM whole rocks become zircon saturated based on their Zr con-tent and zircon saturation models of Watson and Harrison (1983) and Boehnke et al. (2013) (Andersen et al. 2017). In addition, the trace element concentrations (e.g., REE, U, Hf, Ti contents, Eu/Gd) of younger rdm zircons are also within those that were previously observed for rdm zircons (Andersen et al. 2019) (Fig. 7). Following the same reason-ing, rle zircon trace element composition and $^{230}Th$-$^{238}U$ ages (Andersen et al. 2019) (Fig. 7) and the rle MIZ compo-sition (Figs. 4 and S6) supports the notion of their formation from the magmatic system that underlies the LdM. Hence, the younger rdm and rle zircons in this study formed from melts in a growing crystal mush over a significant part of its 60 kyr history (based on the oldest zircon ages of Andersen et al. (2019)), and the MIZs hosted in these zircons record the compositions and storage depths of the zircon-saturated regions within the crystal mush melt over time. In order to correlate the $^{238}U$–$^{230}Th$ age from the host zircon with the MIZ composition, uncertainties associated with the placement of the age spots relative to the location of the MIZs within the host zircon were considered. We used the CL images of the host zircon (Fig. S1-1) to determine if an

age spot can be considered to date the (1) age of the MIZ entrapment (when the age spot is directly in the same CL domain as the MIZ), or should rather be considered to date the (2) minimum or (3) maximum age of the MIZ entrap-ment (depending on whether the age spot is in a CL domain that is further away from (i.e., min. age) or closer to (i.e., max. age) the zircon core than the MIZ (refer to the caption of Fig. 8 for details)).

The younger rdm and rle MIZ compositions record relatively homogeneous crystal mush melt composition during its buildup (Fig. 8) that is consistent with the post-glacial silicic whole rock data (Fig. 4). However, there are compositional differences between the younger rdm and rle MIZs. The younger rdm MIZs are on average less differentiated (e.g., lower $SiO_2$, higher $Al_2O_3$ and MgO) than the rle MIZs (Fig. 8), and this difference is observed from at least $\sim 30$ kyr before eruption until close to the eruption ages of both units (19 to 23 ka) (Fig. 8). Less evolved rdm MIZ compared to rle MIZ is consistent with the hypothesis that the rdm crystal mush was better connected to the deeper mid-crustal plumbing system than the rle crystal mush, as proposed by Klug et al. (2020) based on the less evolved rdm plagioclase melt inclusion with deeper entrapment depths as compared to those of rle. While the plagioclase melt inclusions were entrapped only decades to centuries before eruption (Andersen et al. 2018), MIZs record a persistent difference between rdm and rle going back to $\sim 30$ kyr before eruption, suggesting the long-term connection of the rdm crystal mush to deeper depths (higher T and lesser degree of plagioclase/zircon fractionation) than that of the rle.

The magma storage pressures recorded by the entrapment pressures of younger rdm MIZs are 1.1 to 2.8 kbars (4.0 to 10.5 km depth) (Fig. 9), based on their $H_2O$ contents, assumed range of $CO_2$ content of 0 to 570 ppm (based on the plagioclase-hosted melt inclusions from the rdm unit), and the MagmaSat model of Ghiorso and Gualda (2015) implemented in the VesiCal v1.01 software (Iacovino et al. 2021). There is no clear correlation between the storage pressure and the MIZ entrapment age for the younger rdm MIZs (Fig. 9). The magma storage pressures are consistent with those recorded by the silicic plagioclase-hosted melt inclusions from the rdm unit (1.6 to 2.4 kbars) (Klug et al. 2020) that formed decades to centuries before the eruption of the rdm unit based on the disequilibrium trace element profiles (Andersen et al. 2018). Similar to the rdm MIZs, the rle MIZs record magma storage pressures of 1.4 to 2.8 kbars (5.3 to 10.4 km depth) (assuming MIZ $CO_2$ of 25 to 344 ppm based on the plagioclase-hosted melt inclusions from the rle unit) that match well with those recorded by the rle plagioclase melt inclusions (1.7 to 2.2 kbars) (Klug et al. 2020). The magma storage pressure recorded by the rle MIZs appears to decrease through time (Fig. 9), but the significance of this trend is unclear given the small number

**Fig. 8** Major element composition of the rdm and rle MIZs vs. their entrapment ages estimated based on the $^{238}U$–$^{230}Th$ age data of the host zircons. The vertical light-red bar shows the eruption age of rdm and rle units (Andersen et al. 2017). As discussed in Sect. "Major Element Composition and H$_2$O Contents of the Younger rdm and rle MIZs: Implications for the LdM Magmatic System", some $^{238}U$–$^{230}Th$ age spots should be considered to be the minimum (i.e., age spot in CL domain further away from zircon core than that of the MIZ) or maximum (i.e., age spot in CL domain closer to zircon core than that of the MIZ) entrapment ages of the MIZs. In such cases, we estimated the maximum or minimum MIZ entrapment ages based on

the mean age difference between the zircon rim and interior ages of the rdm (8.5 kyr) and rle (13.9 kyr) zircons (Andersen et al. 2019). For example, if the age spot is in a CL domain that is closer to the zircon core than the CL domain that the MIZ is in (e.g., rdm-1 i1, Fig. S1-1), the $^{238}U$–$^{230}Th$ age $(47.0^{+4.0}_{-3.9}$ ka) was considered the maximum age of MIZ entrapment and the minimum age was estimated by subtracting the mean age difference between the zircon rim and interior ages of the rdm (8.5 kyr) zircons (Andersen et al. 2019) from the negative uncertainty of the $^{238}U$–$^{230}Th$ age (entrapment age = $(47.0^{+4.0}_{-12.4}$ ka)

of MIZs. The agreement between the magma storage pressures recorded by the MIZs and the plagioclase-hosted melt inclusions suggests that the storage depths of evolved melts that are zircon- (+ plagioclase- ± quartz-) saturated were relatively constant from the time of MIZ entrapment (younger rdm and rle zircon ages of 18.7 to 47.0 ka and 19.7 to 55.8 ka, respectively) until the time of rdm and rle eruption (plagioclase age of decades to centuries before eruption at 19 to 23 ka for rdm and 19 ± 0.4 ka for rle). The magma storage pressures of 1.1 to 2.8 kbars recorded by younger rdm and rle MIZs are consistent with the optimal emplacement window (2.0 ± 0.5 kbar) of silicic magma reservoir growth, storage, and eruptibility based on the thermomechanical model of Huber et al. (2019).

# Conclusion

The study of MIZs from the Laguna del Maule volcanic field provides unique insights into the structure and evolution of silicic magmatic systems. MIZs extend the record of magma compositions back to ~ 30 kyr before the eruption,

providing important constraints on the age, storage depth, temperature, and composition of magmas. We observe a long-term difference in zircon-saturated melt composition between the rdm and rle eruption units, with the rdm MIZs indicating a less evolved crystal mush than that of the rle. These findings suggest the that since ~ 30 kyr before eruption, the rdm crystal mush was better connected to a deeper and more primitive magma body than the rle crystal mush. The correlation between SiO$_2$ and H$_2$O contents observed in the MIZs suggests that the H$_2$O contents of the MIZs are not significantly affected by diffusion of H through the host zircon. The rdm and rle MIZs record magma storage pressures of 1.1 to 2.8 kbars that are consistent with the optimal emplacement window (2.0 ± 0.5 kbar) of silicic magma reservoir growth, storage, and eruptibility based on thermomechanical model of Huber et al. (2019).
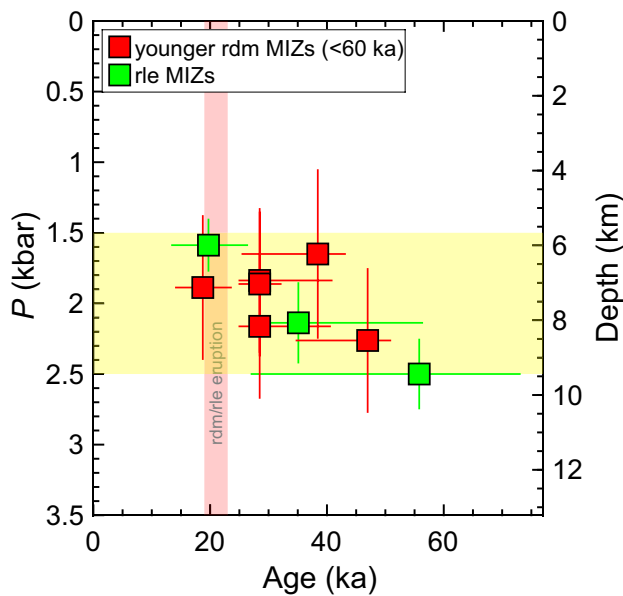
**Fig. 9** Magma storage pressures recorded by the rdm and rle MIZs vs. their entrapment ages estimated based on the $^{238}U$–$^{230}Th$ age data of the host zircons. The pressures were calculated based on the MIZ $H_2O$ contents, ranges of MIZ $CO_2$ content assumed based on plagioclase-hosted melt inclusion data (Klug et al. 2020) (0 to 570 ppm and 25 to 344 ppm for rdm and rle MIZs respectively) and the MagmaSat model of Ghiorso and Gualda (2015) implemented in the Vesi-Cal v1.01 software (Iacovino et al. 2021). The vertical light-red bar shows the eruption age of rdm and rle units (Andersen et al. 2017). The horizontal light-yellow bar indicates the optimal emplacement window ($2.0 \pm 0.5$ kbar) of silicic magma reservoir growth, storage, and eruptibility based on thermomechanical model of Huber et al. (2019). Depth on the right axis is calculated with a crustal density of 2,700 kg/m$^3$. For the description of the uncertainties in the MIZ entrapment ages, refer to Sect. "Major Element Composition and $H_2O$ Contents of the Younger rdm and rle MIZs: Implications for the LdM Magmatic System" and caption of Fig. 8

# References

Andersen NL, Singer BS, Jicha BR, Beard BL, Johnson CM, Licciardi JM (2017) Pleistocene to holocene growth of a large upper crustal rhyolitic magma reservoir beneath the active Laguna del Maule volcanic field, central Chile. J Petrol 58(1):85–114. https://doi.org/10.1093/petrology/egx006

Andersen NL, Singer BS, Costa F, Fournelle J, Herrin JS, Fabbro GN (2018) Petrochronologic perspective on rhyolite volcano unrest at Laguna del Maule, Chile. Earth Planet Sci Lett 493:57–70. https://doi.org/10.1016/j.epsl.2018.03.043

Andersen NL, Singer BS, Coble MA (2019) Repeated rhyolite eruption from heterogeneous hot zones embedded within a cool shallow magma reservoir. J Geophys Res Solid Earth 124(3):2582–2600. https://doi.org/10.1029/2018jb016418

Bachmann O, Bergantz GW (2004) On the origin of crystal-poor rhyolites: extracted from batholithic crystal mushes. J Petrol 45(8):1565–1582

Bachmann O, Bergantz GW (2006) Gas percolation in upper-crustal silicic crystal mushes as a mechanism for upward heat advection and rejuvenation of near-solidus magma bodies. J Volcanol Geoth Res 149(1–2):85–102

Bai T, Thurber C, Lanza F, Singer BS, Bennington N, Keranen K, Cardona C (2020) Teleseismic tomography of the Laguna del Maule volcanic field in Chile. J Geophys Res 125(8):e2020JB019449

Barboni M, Boehnke P, Schmitt AK, Harrison TM, Shane P, Bouvier AS, Baumgartner L (2016) Warm storage for arc magmas. Proc Natl Acad Sci 113(49):13959–13964. https://doi.org/10.1073/pnas.1616129113

Barker S, Wilson C, Smith EG, Charlier B, Wooden JL, Hiess J, Ireland T (2014) Post-supereruption magmatic reconstruction of Taupo volcano (New Zealand), as reflected in zircon ages and trace elements. J Petrol 55(8):1511–1533

Barth AP, Wooden JL (2010) Coupled elemental and isotopic analyses of polygenetic zircons from granitic rocks by ion microprobe, with implications for melt evolution and the sources of granitic magmas. Chem Geol 277(1–2):149–159

Bindeman IN, Simakin AG (2014) Rhyolites—Hard to produce, but easy to recycle and sequester: Integrating microgeochemical observations and numerical models. Geosphere 10(5):930–957

Bindeman IN, Fu B, Kita NT, Valley JW (2008) Origin and evolution of silicic magmatism at Yellowstone based on ion microprobe analysis of isotopically zoned zircons. J Petrol 49(1):163–193

Blum TB, Kitajima K, Kita N, Valley JW (2023) Analysis of trace elements in zircon at high mass resolving power using forward-geometry secondary ion mass spectrometry. In: Goldschmidt 2023 Conference Proceedings

Blundy J, Cashman K (2005) Rapid decompression-driven crystallization recorded by melt inclusions from Mount St. Helens Volcano. Geology 33(10):793–796

Blundy J, Cashman K (2008) Petrologic reconstruction of magmatic system variables and processes. RiMG 69(1):179–239

Bodnar R, Student JJ (2006) Melt inclusions in plutonic rocks: petrography and microthermometry. In: Webster JD (ed) Melt inclusions in plutonic rocks, vol 36. Montreal, Quebec, pp 1–25

Boehnke P, Watson EB, Trail D, Harrison TM, Schmitt AK (2013) Zircon saturation re-revisited. Chem Geol 351:324–334

Bouvier A-S, Ushikubo T, Kita NT, Cavosie AJ, Kozdon R, Valley JW (2012) Li isotopes and trace elements as a petrogenetic tracer in zircon: insights from Archean TTGs and sanukitoids. Contrib Mineral Petr 163:745–768

Bucholz CE, Jagoutz O, VanTongeren JA, Setera J, Wang Z (2017) Oxygen isotope trajectories of crystallizing melts: insights from modeling and the plutonic record. Geochim Cosmochim Acta 207:154–184

Cashman KV, Sparks RSJ, Blundy JD (2017) Vertically extensive and unstable magmatic systems: a unified view of igneous processes. Science 355(6331):3055

Chamberlain KJ, Wilson CJN, Wooden JL, Charlier BLA, Ireland TR (2014) New perspectives on the bishop tuff from zircon textures,

ages and trace elements. J Petrol 55(2):395–426. https://doi.org/10.1093/petrology/egt072

Charlier B, Wilson C (2010) Chronology and evolution of caldera-forming and post-caldera magma systems at Okataina Volcano, New Zealand from zircon U-Th model-age spectra. J Petrol 51(5):1121–1141

Cheng H, Edwards RL, Shen C-C, Polyak VJ, Asmerom Y, Woodhead J, Hellstrom J, Wang Y, Kong X, Spötl C (2013) Improvements in $^{230}$Th dating, $^{230}$Th and $^{234}$U half-life values, and U-Th isotopic measurements by multi-collector inductively coupled plasma mass spectrometry. Earth Planet Sci Lett 371:82–91

Claiborne LL, Miller CF, Flanagan DM, Clynne MA, Wooden JL (2010) Zircon reveals protracted magma storage and recycling beneath Mount St Helens. Geology 38(11):1011–1014

Coble MA, Vazquez JA, Barth AP, Wooden J, Burns D, Kylander-Clark A, Jackson S, Vennari CE (2018) Trace element characterisation of MAD-559 zircon reference material for ion microprobe analysis. Geostand Geoanal Res 42(4):481–497

Contreras C, Cashman KV, Rust A, Cortés M (2022) The influence of magma storage and ascent conditions on Laguna del Maule rhyolite eruptions. J Petrol 63(12):121

Cooper KM, Kent AJR (2014) Rapid remobilization of magmatic crystals kept in cold storage. Nature 508(7497):554–554. https://doi.org/10.1038/nature13280

Cordell D, Unsworth MJ, Diaz D (2018) Imaging the Laguna del Maule Volcanic Field, central Chile using magnetotellurics: Evidence for crustal melt regions laterally-offset from surface vents and lava flows. Earth Planet Sci Lett 488:168–180. https://doi.org/10.1016/j.epsl.2018.01.007

Cordell D, Unsworth MJ, Diaz D, Reyes-Wagner V, Currie CA, Hicks SP (2019) Fluid and melt pathways in the central chilean subduction zone near the 2010 Maule earthquake (35–36°S) as inferred from magnetotelluric data. Geochem Geophys Geosys 20(4):1818–1835. https://doi.org/10.1029/2018gc008167

Crowley JL, Schoene B, Bowring S (2007) U-Pb dating of zircon in the Bishop Tuff at the millennial scale. Geology 35(12):1123–1126

Danyushevsky LV, Sokolov S, Falloon TJ (2002) Melt inclusions in olivine phenocrysts: using diffusive re-equilibration to determine the cooling history of a crystal, with implications for the origin of olivine-phyric volcanic rocks. J Petrol 43(9):1651–1671

Donovan JJ, Singer JW, Armstrong JT (2016) A new EPMA method for fast trace element analysis in simple matrices. Am Mineral 101(8):1839–1853

Eiler JM, Crawford A, Elliott T, Farley KA, Valley JW, Stolper EM (2000) Oxygen isotope geochemistry of oceanic-arc lavas. J Petrol 41(2):229–256

Feigl KL, Le Mével H, Tabrez Ali S, Córdova L, Andersen NL, DeMets C, Singer BS (2014) Rapid uplift in Laguna del Maule volcanic field of the Andean Southern Volcanic zone (Chile) 2007–2012. Geophys J Int 196(2):885–901

Ferry JM, Watson EB (2007) New thermodynamic models and revised calibrations for the Ti-in-zircon and Zr-in-rutile thermometers. Contrib Mineral Petr 154(4):429–437. https://doi.org/10.1007/s00410-007-0201-0

Fierstein J (2018) Postglacial eruptive history established by mapping and tephra stratigraphy provides perspectives on magmatic system beneath Laguna del Maule, Chile. In: AGU Chapman Conference, Integrating Geophysical, Petrochronologic, and Modeling Perspectives on Large Silicic Magma Systems, Quinamavida, Chile January, vol., pp 7–12

Ghiorso MS, Evans BW (2008) Thermodynamics of rhombohedral oxide solid solutions and a revision of the Fe-Ti two-oxide geothermometer and oxygen-barometer. Am J Sci 308(9):957–1039

Ghiorso MS, Gualda GA (2015) An $H_2O$–$CO_2$ mixed fluid saturation model compatible with rhyolite-MELTS. Contrib Mineral Petr 169:1–30

Grimes CB, Ushikubo T, John BE, Valley JW (2011) Uniformly mantle-like δ$^{18}$O in zircons from oceanic plagiogranites and gabbros. Contrib Mineral Petr 161:13–33

Grimes CB, Wooden JL, Cheadle MJ, John BE (2015) Fingerprinting tectono-magmatic provenance using trace elements in igneous zircon. Contrib Mineral Petr. https://doi.org/10.1007/s00410-015-1199-3

Hildreth W (2004) Volcanological perspectives on Long Valley, Mammoth Mountain, and Mono Craters: several contiguous but discrete systems. J Volcanol Geoth Res 136(3–4):169–198. https://doi.org/10.1016/j.jvolgeores.2004.05.019

Hildreth W, Godoy E, Fierstein J, Singer B (2010) Laguna del Maule volcanic field: Eruptive history of a Quaternary basalt-to-rhyolite distributed volcanic field on the Andean rangecrest in central Chile. In, vol. Servicio Nacional de Geología y Minería,

Huber C, Parmigiani A (2018) A physical model for three-phase compaction in silicic magma reservoirs. J Geophys Res 123(4):2685–2705

Huber C, Townsend M, Degruyter W, Bachmann O (2019) Optimal depth of subvolcanic magma chamber growth controlled by volatiles and crust rheology. Nat Geosci 12(9):762

Iacovino K, Matthews S, Wieser PE, Moore G, Bégué F (2021) VESIcal Part I: An open-source thermodynamic model engine for mixed volatile ($H_2O$-$CO_2$) solubility in silicate melts. Earth and Space Science 8(11):e2020EA001584

Ireland TR, Williams IS (2003) Considerations in zircon geochronology by SIMS. RiMG 53(1):215–241

Jaffey AH, Flynn KF, Glendenin LE, Bentley WC, Essling AM (1971) Precision measurement of half-lives and specific activities of 235U and 238U. Physical review C 4(5):1889–1906

Jochum KP, Stoll B, Herwig K, Willbold M, Hofmann AW, Amini M, Aarburg S, Abouchami W, Hellebrand E, Mocek B (2006) MPI-DING reference glasses for in situ microanalysis: New reference values for element concentrations and isotope ratios. Geochem Geophys Geosyst 7(2)

Kelly JL, Fu B, Kita NT, Valley JW (2007) Optically continuous silcrete quartz cements of the St. Peter Sandstone: High precision oxygen isotope analysis by ion microprobe. Geochim Cosmochim Acta 71(15):3812–3832

Kita NT, Ushikubo T, Fu B, Valley JW (2009) High precision SIMS oxygen isotope analysis and the effect of sample topography. Chem Geol 264(1–4):43–57

Kitajima K, Ushikubo T, Kita NT, Maruyama S, Valley JW (2012) Relative retention of trace element and oxygen isotope ratios in zircon from archean rhyolite, panorama formation, north pole dome, pilbara craton, Western Australia. Chem Geol 332:102–115

Klug JD, Singer BS, Kita NT, Spicuzza MJ (2020) Storage and evolution of laguna del maule rhyolites: insight from volatile and trace element contents in melt inclusions. J Geophys Res SolidEarth. https://doi.org/10.1029/2020JB019475

Kress VC, Ghiorso MS (2004) Thermodynamic modeling of post-entrapment crystallization in igneous phases. J Volcanol Geoth Res 137(4):247–260

Lackey JS, Valley JW, Chen JH, Stockli DF (2008) Dynamic magma systems, crustal recycling, and alteration in the central Sierra Nevada batholith: the oxygen isotope record. J Petrol 49(7):1397–1426

Le Mevel H, Feigl KL, Cordova L, DeMets C, Lundgren P (2015) Evolution of unrest at Laguna del Maule volcanic field (Chile) from InSAR and GPS measurements, 2003 to 2014. Geophys Res Lett 42(16):6590–6598. https://doi.org/10.1002/2015gl064665

Le Mevel H, Gregg PM, Feigl KL (2016) Magma injection into a long-lived reservoir to explain geodetically measured uplift: Application to the 2007–2014 unrest episode at Laguna del Maule volcanic field, Chile. J Geophys Res Solid Earth 121(8):6092–6108. https://doi.org/10.1002/2016jb013066

Le Mével H, Córdova L, Cardona C, Feigl K (2021) Unrest at the Laguna del Maule volcanic field 2005–2020: renewed acceleration of deformation. Bull Volcanol 83(6):39

Ludwig K (2001) Squid (1.13 b). A user's manual: Berkeley Geochronology Center Special Publication 2

Ludwig KR (2003) Isoplot (3.41d), a geochronological toolkit for Excel. A user's manual: Berkeley Geochronology Center Special Publication 4

Mahood G (1990) Second reply to comment of RSJ Sparks, HE Huppert and CJN Wilson on "Evidence for long residence times of rhyolitic magma in the Long Valley magmatic system: the isotopic record in the precaldera lavas of Glass Mountain." Earth Planet Sci Lett 99(4):395–399

McDonough WF, Sun S-S (1995) The composition of the Earth. Chem Geol 120(3–4):223–253

Miller CA, Williams-Jones G, Fournier D, Witter J (2017) 3D gravity inversion and thermodynamic modelling reveal properties of shallow silicic magma reservoir beneath Laguna del Maule, Chile. Earth Planet Sci Lett 459:14–27

Morgan GB, London D (2005) Effect of current density on the electron microprobe analysis of alkali aluminosilicate glasses. Am Mineral 90(7):1131–1138

Nasdala L, Corfu F, Schoene B, Tapster SR, Wall CJ, Schmitz MD, Ovtcharova M, Schaltegger U, Kennedy AK, Kronz A (2018) GZ 7 and GZ 8–two zircon reference materials for SIMS U-Pb geochronology. Geostand Geoanal Res 42(4):431–457

Newman S, Stolper EM, Epstein S (1986) Measurement of water in rhyolitic glasses; calibration of an infrared spectroscopic technique. Am Mineral 71(11–12):1527–1541

Newman S, Epstein S, Stolper E (1988) Water, carbon dioxide, and hydrogen isotopes in glasses from the ca. 1340 AD eruption of the Mono Craters, California: Constraints on degassing phenomena and initial volatile content. J Volcanol Geoth Res 35(1–2):75–96

Page FZ, Fu B, Kita NT, Fournelle J, Spicuzza MJ, Schulze DJ, Viljoen F, Basei MA, Valley JW (2007) Zircons from kimberlite: new insights from oxygen isotopes, trace elements, and Ti in zircon thermometry. Geochim Cosmochim Acta 71(15):3887–3903

Pearce NJ, Perkins WT, Westgate JA, Gorton MP, Jackson SE, Neal CR, Chenery SP (1997) A compilation of new and published major and trace element data for NIST SRM 610 and NIST SRM 612 glass reference materials. Geostand Newsl 21(1):115–144

Peres P, Kita NT, Valley JW, Fernandes F, Schuhmacher M (2013) New sample holder geometry for high precision isotope analyses. Surf Interface Anal 45(1):553–556

Qin Z, Lu F, Anderson AT (1992) Diffusive reequilibration of melt and fluid inclusions. Am Mineral 77(5–6):565–576

Reid MR, Vazquez JA, Schmitt AK (2011) Zircon-scale insights into the history of a Supervolcano, Bishop Tuff, Long Valley, California, with implications for the Ti-in-zircon geothermometer (vol 161, pg 293. Contrib Mineral Petr 161(2):313–314. https://doi.org/10.1007/s00410-010-0564-5

Reid MR, Vazquez JA (2017) Fitful and protracted magma assembly leading to a giant eruption, Youngest Toba Tuff Indonesia. Geochem Geophys Geosys 18(1):156–177

Roedder E (1984) Volume 12: Fluid Inclusions. Rev Mineral 12:644

Rose-Koga E, Bouvier A-S, Gaetani GA, Wallace P, Allison C, Andrys J, De La Torre CA, Barth A, Bodnar R, Gartner AB et al. (2021) Silicate melt inclusions in the new millennium: a review of recommended practices for preparation, analysis, and data presentation. Chem Geol 570:120145

Rubin AE, Cooper KM, Till CB, Kent AJ, Costa F, Bose M, Gravley D, Deering C, Cole J (2017) Rapid cooling and cold storage in a silicic magma reservoir recorded in individual crystals. Science 356(6343):1154–1156

Sano Y, Terada K, Fukuoka T (2002) High mass resolution ion microprobe analysis of rare earth elements in silicate glass, apatite and zircon: lack of matrix dependency. Chem Geol 184(3–4):217–230

Schaen AJ, Singer BS, Cottle JM, Garibaldi N, Schoene B, Satkoski AM, Fournelle J (2018) Textural and mineralogical record of low-pressure melt extraction and silicic cumulate formation in the late Miocene Risco Bayo-Huemul plutonic complex, southern Andes. J Petrol 59(10):1991–2016

Schaen AJ, Schoene B, Dufek J, Singer BS, Eddy MP, Jicha BR, Cottle JM (2021) Transient rhyolite melt extraction to produce a shallow granitic pluton. Sci Adv 7(21):0604

Singer BS, Hildreth W, Vincze Y (2000) $^{40}Ar/^{39}Ar$ evidence for early deglaciation of the central Chilean Andes. Geophys Res Lett 27(11):1663–1666

Singer BS, Andersen NL, Le Mével H, Feigl KL, DeMets C, Tikoff B, Thurber CH, Jicha BR, Cardona C, Córdova L (2014a) Dynamics of a large, restless, rhyolitic magma system at Laguna del Maule, southern Andes Chile. GSA Today 24(12):4–10

Singer BS, Jicha BR, Fournelle JH, Beard BL, Johnson CM, Smith KE, Greene SE, Kita NT, Valley JW, Spicuzza MJ (2014b) Lying in wait: deep and shallow evolution of dacite beneath Volcán de Santa María, Guatemala. Geological Society, London, Special Publications 385(1):209–234

Singer BS, Le Mével H, Licciardi JM, Córdova L, Tikoff B, Garibaldi N, Andersen NL, Diefenbach AK, Feigl KL (2018) Geomorphic expression of rapid Holocene silicic magma reservoir growth beneath Laguna del Maule Chile. Sci Adv 4(6):1513

Sobolev V, Kostyuk V (1975) Magmatic crystallization based on a study of melt inclusions. Fluid Inclusion Res 9:182–253

Steiger RH, Jäger E (1977) Subcommission on geochronology: convention on the use of decay constants in geo-and cosmochronology. Earth Planet Sci Lett 36(3):359–362

Stelten ME, Cooper KM (2012) Constraints on the nature of the sub-volcanic reservoir at South Sister volcano, Oregon from U-series dating combined with sub-crystal trace-element analysis of plagioclase and zircon. Earth Planet Sci Lett 313:1–11

Szymanowski D, Wotzlaw JF, Ellis BS, Bachmann O, Guillong M, von Quadt A (2017) Protracted near-solidus storage and pre-eruptive rejuvenation of large magma reservoirs. Nat Geosci 10(10):777

Thomas J, Bodnar R, Shimizu N, Chesner C (2003) Melt inclusions in zircon. RiMG 53(1):63–87

Valley JW, Kita NT (2009) In situ oxygen isotope geochemistry by ion microprobe. MAC Short Course 41:19–63

Valley JW, Lackey JS, Cavosie AJ, Clechenko CC, Spicuzza MJ, Basei MAS, Bindeman IN, Ferreira VP, Sial AN, King EM (2005) 4.4 billion years of crustal maturation: oxygen isotope ratios of magmatic zircon. Contrib Mineral Petr 150(6):561–580

Valley JW, Kitajima K, Spicuzza MJ, Blum TB, Kita NT (2024) UWZ1, A Zircon Standard for Oxygen Isotope Analysis by SIMS: IMF Revisited. Goldschmidt Conf, Chicago

Wallace PJ (2005) Volatiles in subduction zone magmas: concentrations and fluxes based on melt inclusion and volcanic gas data. J Volcanol Geoth Res 140(1–3):217–240

Wallace PJ, Anderson AT, Davis AM (1999) Gradients in $H_2O$, $CO_2$, and exsolved gas in a large-volume silicic magma system: Interpreting the record preserved in melt inclusions from the Bishop Tuff. J Geophys Res SolidEarth 104(B9):20097–20122

Wang X-L, Coble MA, Valley JW, Shu X-J, Kitajima K, Spicuzza MJ, Sun T (2014) Influence of radiation damage on late jurassic zircon from southern China: Evidence from in situ measurements of oxygen isotopes, laser Raman, U-Pb ages, and trace elements. Chem Geol 389:122–136

Watson EB, Harrison TM (1983) Zircon saturation revisited: temperature and composition effects in a variety of crustal magma types. Earth Planet Sci Lett 64(2):295–304

Wespestad CE, Thurber CH, Andersen NL, Singer BS, Cardona C, Zeng XF, Bennington NL, Keranen K, Peterson DE, Cordell D, Unsworth M, Miller C, Williams-Jones G (2019) Magma reservoir below laguna del maule volcanic field, Chile imaged with surface-wave tomography. J Geophys Res SolidEarth 124(3):2858–2872. https://doi.org/10.1029/2018jb016485

Wiedenbeck M, Hanchar JM, Peck WH, Sylvester P, Valley JW, Whitehouse MJ, Kronz A, Morishita Y, Nasdala L, Fiebig J (2004) Further characterisation of the 91500 zircon crystal. Geostand Geoanal Res 28(1):9–39

Williams IS (1997) U-Th-Pb geochronology by ion microprobe. In: McKibben MA, Shanks III WC, Ridley WI (eds) Application of microanalytical techniques to understanding mineralizing processes, vol 7. Reviews in Economic Geology, Society of Economic Geologists, pp 1–35

Wilson CJN, Charlier BLA (2009) Rapid rates of magma generation at contemporaneous magma systems, Taupo volcano, New Zealand: insights from U-Th model-age spectra in zircons. J Petrol 50(5):875–907. https://doi.org/10.1093/petrology/egp023

Wolff JA, Ellis B, Ramos FC, Starkel WA, Boroughs S, Olin PH, Bachmann O (2015) Remelting of cumulates as a process for producing chemical zoning in silicic tuffs: A comparison of cool, wet and hot, dry rhyolitic magma systems. Lithos 236:275–286

Wotzlaw JF, Bindeman IN, Stern RA, D'Abzac FX, Schaltegger U (2015) Rapid heterogeneous assembly of multiple magma reservoirs prior to Yellowstone supereruptions. Sci Rep 5:14026